On the in-situ aqueous stability of an Mg-Li-(Al-Y-Zr) alloy: Role of Li

Y.M. Yan, A. Maltseva, P. Zhou, X.J. Li, Z.R. Zeng, O. Gharbi, K. Ogle, M. La Haye, M. Vaudescal, M. Esmaily, et al.

▶ **To cite this version:**

Y.M. Yan, A. Maltseva, P. Zhou, X.J. Li, Z.R. Zeng, et al.. On the in-situ aqueous stability of an Mg-Li-(Al-Y-Zr) alloy: Role of Li. Corrosion Science, 2020, 164, pp.108342 -. 10.1016/j.corsci.2019.108342 . hal-03489503

HAL Id: hal-03489503
https://hal.science/hal-03489503

Submitted on 7 Mar 2022

HAL is a multi-disciplinary open access archive for the deposit and dissemination of scientific research documents, whether they are published or not. The documents may come from teaching and research institutions in France or abroad, or from public or private research centers.

L'archive ouverte pluridisciplinaire **HAL**, est destinée au dépôt et à la diffusion de documents scientifiques de niveau recherche, publiés ou non, émanant des établissements d'enseignement et de recherche français ou étrangers, des laboratoires publics ou privés.

Distributed under a Creative Commons Attribution - NonCommercial 4.0 International License

Version of Record: https://www.sciencedirect.com/science/article/pii/S0010938X19319390
Manuscript_bd0d84c0afcdfb6703c86df3d5c1a5d1

On the in-situ aqueous stability of an Mg-Li-(Al-Y-Zr) alloy: Role of Li

Y.M. Yan[a,b,†], A, Maltseva[b,†], P. Zhou[b,c], X.J. Li[b], Z.R. Zeng[a], O. Gharbi[d], K. Ogle[b], M. La Haye[f], M. Vaudescal[f], M. Esmaily[a], N. Birbilis[e] and P. Volovitch*[, b]

[a]*Department of Materials Science and Engineering, Monash University, VIC 3800, Australia.*
[b]*Chimie ParisTech, PSL Research University, CNRS, Institut de Recherche de Chimie Paris (IRCP), F-75005 Paris, France*
[c]*Shenyang National Laboratory for Materials Science, Northeastern University, Shenyang, 110819, China*
[d]*Sorbonne Université, CNRS, Laboratoire Interfaces et Systèmes Electrochimiques, LISE, F-75005 Paris, France*
[e]*College of Engineering and Computer Science, Australian National University, ACT 2601, Australia*
[f]*PLACAMAT, 87 avenue Docteur Albert Schweitzer, 33608 PESSAC Cedex, France*

*Corresponding authors:

polina.volovitch@chimieparistech.psl.eu (P. Volovitch) / Tel: +33 66136 6823

†These authors contributed equally.

Abstract

The aqueous stability of a corrosion resistant Mg-Li(-Al-Y-Zr)-alloy was investigated by combining in-situ confocal Raman Microscopy, Atomic Emission SpectroElectroChemistry, ex-situ Photoluminiscence Spectroscopy, Auger Electron Spectroscopy and Glow Discharge Optical Emission Spectroscopy. Li and Mg dissolved from visually intact anodic areas, leaving a Li-depleted metallic layer under approximately 100 nm thick Li-doped MgO. The transformation $MgO \rightarrow Mg(OH)_2$ was inhibited. $Li_2[Al_2(OH)_6]_2 \cdot CO_3 \cdot nH_2O$, $LiAlO_2$, Y_2O_3 and $Mg(OH)_2$ accumulated locally around active cathodic sites. New corrosion mechanism is proposed, which associates the improved corrosion resistance of Mg-Li alloys with an enhanced chemical stability and modified catalytic activity of MgO in presence of Li^+.

Keywords: A. Magnesium; B. in-situ Raman spectroscopy; B. ICP-OES; B. AES (Auger spectroscopy); C. Interfaces; C. Neutral inhibition

© 2019 published by Elsevier. This manuscript is made available under the CC BY NC user license
https://creativecommons.org/licenses/by-nc/4.0/

Introduction

Magnesium-Lithium (Mg-Li) alloys offer great potential as ultra-lightweight structural materials owing to their exceptionally low-density and room temperature ductility [1-3]. To improve the strength of Mg-Li alloys, the body centred cubic (bcc) binary Mg–Li system requires ternary and quaternary alloying additions [4-8]. Hence, an alloy based on the Mg-Li(-Al-Y-Zr) has recently been studied, which contains ~11 wt. % (equivalent to 33 at. %) Li, exhibiting a unique exceptional combination of strength, ductility, in addition to corrosion resistance [9]. The minor alloying additions of aluminium (Al), yttrium (Y) and zirconium (Zr) provide enhanced mechanical properties through the formation of dispersoids and semi-coherent nanosized precipitates. *Comparing corrosion performance of Mg-Al and Mg-RE alloys with the studied in this work optimized alloy, one may note significant decrease in corrosion currents of the studied alloy (Figure 1 in [9]). Considering Mg-Zr alloys, reviewed in [10] their corrosion currents are in the range of 20 to 100 µA cm^{-2}, which is in any case higher than the corrosion current of Mg-Li(-Al-Y-Zr), reported in [9] as low as 6 µA cm^{-2}.*

As described in the literature [11, 12], the principal alloying element (Li), plays several roles in the alloys properties, namely: enhancing Mg ductility through altering the Mg hexagonal close packed (hcp) crystal structure to bcc; decreasing alloy density (ρ = 0.535 for Li, vs. 1.738 g/cm^3 for Mg); and significantly improving the corrosion performance [9].

The appreciable corrosion resistance of bcc Mg-Li alloys, which is atypical for Mg-alloys, has been demonstrated in aqueous solutions using electrochemical measurements inclusive of potentiodynamic polarisation and impedance spectroscopy (EIS), in addition to physical measurements including hydrogen collection and mass loss testing [9]. Through an extensive microstructural and electrochemical characterisation, it was proposed by Xu et al. [9] that the corrosion resistance of the bcc Mg-Li based system is associated with two key factors: 1) the homogenous and uniform microstructure beyond the nanoscale, and 2) the formation of a protective uniform lithium carbonate (Li_2CO_3)-rich layer on alloy surface. The formation of a carbonate-rich layer on the outermost part of the surface film of different Mg-Li alloys has been confirmed by Yan et al. [13] and Zheng et al. [14] using ex-situ characterisation techniques including grazing incidence x-ray diffraction (GIXRD), Raman spectroscopy, X-ray photoelectron spectroscopy (XPS) and most recently, analytical Transmission Electron Microscopy (TEM) [13].

In a subsequent research, Hou et al. [15] investigated the electrochemical response of Mg-Li(-Al-Y-Zr), using on-line Inductively Coupled Plasma - Mass Spectrometry (ICP-MS). The results presented in this work elucidated the so-called incongruent dissolution at surface of the alloy, indicating a selective detection of Mg

downstream in response to open circuit immersion and under anodic polarisation, which was interpreted as evidence for the accumulation of Li-rich surface products. Recently, by monitoring the ion release using an Inductively Coupled Plasma - Atomic Emission Spectrometer (ICP-AES), Yan et al. [16] reported a rapid re-passivation (which is synonymous with the re-establishment of a surface film) upon the Mg-Li(-Al-Y-Zr) alloy after the sample surface was scratched. Nonetheless, directly studying the surface film composition and its role in the protection of Mg-Li alloys during aqueous exposure remains largely unexplored, with prior works indicating the need for an analysis supported by in-situ surface characterisation.

With the exception of the commonly observed $MgO/Mg(OH)_2$ films and the aforementioned Li_2CO_3 film, there have also been reports of other corrosion products on the surface of different Mg-Li alloys. For example, there are reports indicating the formation of $Li_2O/LiOH$ on the surface of a binary Mg-Li alloy [17], and $CaO/CaCO_3$ upon a Ca-containing Mg-Li alloy [14, 18] The formation of an Al-containing layer (thus Al-containing corrosion products) and possibly the formation of Mg hydroxy-carbonates in the surface film of an Mg-Li(-Al-Y-Zr) alloy were also reported [13]. As such, the surface chemistry of Mg-Li alloys is expected to be complicated, and to vary with bulk alloy compositions. A recent study of a Mg-Li matrix composite containing Al_2Y, reported Y_2O_3 and Al_2O_3 on the surface [19]. However, the precise nature of Y and Al containing corrosion products, their spatial distribution and their influence on the corrosion resistance has not yet been elaborated for Mg-Li alloys.

Except for the formation of Li-containing corrosion products, the Li addition may also influence the corrosion of Mg-Li alloys by other means. The electronic structure, reactivity and morphology of the MgO film can be altered significantly by Li-doping [20-23]. For instance, addition of Li^+ was reported to be able to efficiently influence the hydration and dehydration rates of MgO [24-26]. Therefore, Li-doping of the $MgO/Mg(OH)_2$ film should be considered as a possibility in the case of Mg-Li alloys.

Whilst acknowledging the considerable efforts in the works cited above, the hypotheses related to corrosion resistance of bcc Mg-Li to date having been principally informed by ex-situ characterisation. The objective of the present work was to attempt to establish the surface film composition and its evolution during aqueous exposure of a Mg-Li(-Al-Y-Zr) alloy containing 30.3% Li, 2.34% Al, 0.128% Y and 0.039% Zr (at%) using combined in-situ surface and solution characterisation and to consider the role of this surface film in corrosion mechanisms.

The dissolution of the Mg-Li(-Al-Y-Zr) alloy during aqueous immersion was studied using Atomic Emission SpectroElectrochemistry (AESEC), combining an electrochemical flow cell with real time solution analysis by ICP-AES. A recently developed in-situ Kinetic Raman Mapping (KRM) approach, consisting of kinetic

measurements in a mapping mode using Confocal Raman Microscope (CRM) [27] was utilised for in-situ characterisation of local chemical and morphological evolution of surface films. Although in-situ confocal Raman spectroscopy can be highly sensitive (detection limits ranging from parts per million (ppm) levels to 0.01 wt. % having been reported for some compounds [28-31]), its sensitivity can vary significantly for different species and acquisition conditions; with some species such as undoped MgO simply not Raman active. For this reason, the in-situ analysis was supplemented by ex-situ Auger Electron Spectroscopy with Scanning Nano Probe (nano-AES) and Glow Discharge Optical Emission Spectroscopy (GD-OES). The analytical capability of these techniques includes depth resolution of several nm, and detection limits on the order of 10^{18} atoms per cm^3 for GD OES and 10^{19} atoms per cm^3 for AES. Additionally, nano-AES permits the local surface characterisation by selection of the analysed zone via live electron imaging.

Materials and Methods

2.1. Materials

A magneisum alloy containing 30.3% Li, 2.34% Al, 0.128% Y and 0.039% Zr (in at%) used for this study was prepared as described elsewhere [16]. *According to the results presented in [9, 13], the alloy is nominally single-phase bcc containing a very fine Li-rich solute nanostructure at typical scale less than several tens of nm, suggesting a homogeneous Li distribution at 50-100 µm scale. The previous work demonstrated also the presence of µm-size Al-Y precipitates. A possible transformation of a small fraction of the bcc alloy into a hcp structure due to a long time ageing at room temperature was mentioned in the later work [13], which could in principle decrease locally Li content in these zones. We however have no data to confirm or decline this hypothesis because the analytical methods used to describe inhomogeneity of alloys at µm to hundreds µm scale, such as XRF and EDS, are not sensitive to light elements and hence are unable to study the distribution of Li in Mg matrix.*

A pure Mg with Fe content less than 50 ppm was used as a reference in some experiments. *The composition of this material can be found in [27] (Table 2, Mg2).* The alloy samples referred as “freshly ground samples” and the reference samples were mechanically prepared by grinding with silicon carbide (SiC) paper from 800 to 4000 grit with ethanol as a lubricant. Subsequently, the samples were cleaned using ethanol in an ultrasonic bath and tested immediately thereafter, limiting the contact with ambient air to less than 20 minutes. Supplementary dissolution tests were made using the samples, referred as “immersed samples”, which were preliminary immersed for 20 hours in 500 mL of 0.01M NaCl aqueous solution.

All the solutions were prepared using analytical grade chemicals (Prolabo) and osmotic water (resistivity 18

MΩ which corresponds to 0.05 μS cm^{-1}). The alloy samples were tested in 0.1 M and 0.01 M NaCl aqueous solutions. The formation of lithium carbonate in the mixture of 0.1 M NaCl+0.1 M Na_2CO_3 solution was also verified for the alloy; the reference samples were tested in 0.1 M NaCl and in 0.1 M LiCl aqueous solutions.

2.2. In-situ solution analysis by AESEC

The AESEC was used to quantitatively monitor in real time the dissolution of Li and Mg with wavelengths 279.55 nm and 670.78 nm consequently, however the evolution of the Y, Zr and Al signals was also verified in a qualitative way, because these elements are present on the polychromator. The complete setup of the AESEC is described elsewhere [32-36]. Briefly, it consisted of an electrochemical flow cell coupled with an Horiba Ultima 2C inductively coupled plasma - atomic emission spectrometer (ICP-AES), enabling simultaneous monitoring of the elemental releases and potential and current [37]. The flow condition was defined by the exposed area of 1.0 cm^2, cell volume 0.2 cm^3 and electrolyte flow rate 2.8 ml min^{-1}, which corresponded to the electrolyte renewal in the cell 14 times per minute. A saturated calomel electrode (SCE) and a platinum plate were used as the reference and the counter electrode respectively. A Gamry Reference 600™ potentiostat was used for the electrochemical tests. The "freshly polished" samples were held at open circuit potential (OCP) for 2000 s then polarised to 200 mV vs OCP.

For the analysis of the dissolution of the surface film formed in long immersion, the solution in which the "immersed" sample was immersed was analysed by ICP OES, than the sample was also tested in the flow cell by AESEC. For this test, the "immersed" sample was analysed at OCP for 2500 s. The sequence was as follows: after 900 s of OCP exposure, the cell was opened and the sample was scratched by a sapphire lancet immediately; then the cell was closed and the ion release after the scratch was also monitored. The sample was glued on the sample holder during the test, in order to guarantee the same exposed to the electrolyte surface area before and after the scratch

2.3. In-situ surface characterisation by confocal Raman spectroscopy

Fresh polished samples were characterised by in-situ confocal Raman spectroscopy in mapping mode (CRM). and the in-situ maps where also used for kinetic Raman Mapping (KRM) using recently proposed methodology [27]. Samples were mounted in a 3D printed acrylonitrile butadiene styrene (ABS) flow cell filled with 0.1 M NaCl. 50 ml of solution was pumping with the flow rate of 8ml/min. Pumping was necessary to evacuate the hydrogen bubbles formed on the sample surface as described elsewhere [27]. The flow rate 8

ml/min was adjusted in a way that (for the used cell volume of 0.57 ml and the exposed area of 3.8 cm^2) the electrolyte renewal was comparable with the AESEC flow condition (the electrolyte in the cell renewed 14 times per minute).

An InVia confocal Raman microscope (Renishaw) was used for collecting the in-situ Raman spectra of the corroded sample surface through the optical window in the flow cell. A green laser (532 nm, 50 mW) and 1800 l/mm grating were used. In-situ spectra were acquired using 20× and 50× (in confocal mode) long distance objectives (NA = 0.4 and 0.5 respectively) and 0.2 s acquisition time in each point. In-situ maps of 200×200 µm with the step of 10 µm were collected for the Raman shift range between 100 and 1750 cm^{-1} and in the range between 2600 and 3900 cm^{-1} in an attempt to achieve an accurate observation of the Li_2CO_3 peak (around 1088 cm^{-1}) and $Mg(OH)_2$ peaks (around 3652 cm^{-1}) [38]. Broad scan spectra were also collected on different areas of the surface with an exposure time of 10 s. At the end of each in-situ measurement the surface was also analysed ex-situ immediately after the electrolyte removal outside the cell and using short distance 100x Leica objective (NA=0.9) in confocal mode with exposure time of 1 s and 10 acquisitions per point.

In order to verify the formation of Li_2CO_3 from aqueous solution the surface was also characterized in situ when reacting in the mixture of 0.1 M NaCl and 0.1 M Na_2CO_3. For the verification of the stability of the air formed Li_2CO_3 film, the surface evolution in 0.1 M NaCl solution was also monitored for the sample which was preliminary pre-corroded in 0.1 M NaCl for 20 hours and air-exposed.

2.4. Ex-situ surface characterisation

2.4.1. GD-OES

Elemental depth profiles were obtained using a GD-Profiler 2^{TM} Glow discharge optical emission spectrometer (Horiba Jobin Yvon) operating with Quantum software. The measurement was made at a power of 17 W and gas pressure 750 Pa. Pure Ar and Ar/ H_2 (1 vol. %) mixture was used as a plasma gas. Depth profiles were monitored using Mg 285 nm, H 122 nm, O 130 nm, Li 671 nm, Al 396 nm, Y 437 and C 156 nm wavelength on the polychromator (focus distance 50 cm). The crater depth measurement was made in-situ using integrated differential interferometry profiling (DiP) system with red lasers (633 nm).

2.4.2. PhotoLuminiscence spectroscopy (PL)

Photoluminescence (PL) spectra were recorded at room temperature (25 °C) with HORIBA Jobin Yvon's LabRAM Raman spectrometer using ultraviolet 325 nm excitation. Li-doped MgO microcrystals are expected to exhibit blue (2.8 eV or 440 nm) and orange (2.1 eV or 580 nm) PL attributed to the bulk oxygen vacancies, or F-type centres, whose emission energy levels are modified by the Li ions incorporated into the MgO

structure and the near oxygen vacancies in the near surface regions consequently [39]. For non-doped MgO, PL emission at 460 nm (2.7 eV) is associated with low coordinated oxygen (holes trapped at Mg ion vacancies acting as acceptor levels) and green PL emission (530-540 nm or 2.3 eV) is associated with a transition from the unpaired electron delocalized over the V-centers.

2.4.3. Depth profiling by Auger Electron Spectroscopy

The distribution of the elements on the oxidized surface and the thickness of the oxide layer were evaluated by Auger Electron Spectroscopy (AES), using a PHI 170 setup and operating at the primary electron beam voltage of 10 kV. A cylindrical mirror analyzer (CMA) with an incident angle of 30° with respect to the surface normal was used and the experiments were performed at a pressure of ~10^{-6} Pa. Depth profiles were carried out with an Ar^+ ion beam sputtering in the following sequence: 7 minutes - surface of 2×2 mm (acquisitions each 30 sec, estimated depth 560 Å) at a voltage of 2 kV, 2.2 µA, then 7 minutes - surface1×1 mm (acquisitions each 30 seconds, estimated depth 1750 Å), 2kV, 2.2 µA, then 10 min – surface of 1×1 mm (acquisitions each minute, estimated depth 5500 Å), 3kV, 3 µA. The spectral windows of all elements of interest were recorded at each acquisition. The equivalent eroded depth at each moment was calculated assuming erosion rate of SiO_2. For this reason, the estimated depth or thickness should be considered as equivalent depth. The interface between the oxide /hydroxide layer and the metal was assumed to be at inflection points on the increasing Mg and decreasing O signals profiles. Mg was monitored in the window 1165-1195 eV, Li from 20 to 75 eV and oxygen at 480-530 eV [40]. To differentiate the chemical state present in the O and Mg peaks, the Target Factor Analysis (TFA) method was used [41]. First, a Principal Component Analysis (PCA) was performed to identify two or three of the most differentiated shapes of the peak and define them as metallic or different oxide type forms. Using the selected peaks, a deconvolution was performed as a function of the erosion depth to determine the concentration of each form of the element in the erosion profile and corroboration between the signals from O and Mg. The presence of the low energy peak of Mg in the region typical for Li^+ complicates the quantitative analysis. Thus, the evolution of Li^+ concentration in the oxide depth was considered in a qualitative way from the comparison of the evolution of Mg^{2+} fraction calculated from the high energy Auger peak area and the evolution of the concentration calculated from the area of the convoluted peak (Li^+ and low energy Mg) in the low energy region.

Results

3.1. Surface evolution from in-situ Confocal Raman Microscopy

The surface evolution of Mg-Li(-Al-Y-Zr) in a thin layer electrolyte was characterised in-situ by Confocal Raman Microscopy (CRM) in kinetic mapping mode (Kinetic Raman Mapping, KRM, [27]). **Fig. 1a** illustrates a typical heterogeneous surface evolution during the immersion of the Mg-Li(-Al-Y-Zr) sample in 0.1 M NaCl aqueous solution (more images can be found in Appendix 1, Fig. S1). A discernible distinction may be made between the areas of cathodic hydrogen evolution (area marked as Type 2 in **Fig. 1a**), the apparently intact surface areas without any visible accumulation of corrosion product (Type 1 "intact" area in **Fig. 1a**) and the developing dark lines resembling crystallographic-like etching (Type 1 "dark" area in **Fig. 1a**).

For immersion times up to 3 - 4 hours, only weak $Mg(OH)_2$ (brucite) peaks were detectable by in-situ confocal Raman on the areas designated as Type 1 (for both, intact and dark areas); while multiple compounds were identified on the active sites of Type 2 (Table 1, see Fig. S2 of Appendix for the detailed spectra).

The identification of the compounds shown in Table 1 at the Type 2 active site reveals the formation of complex and inhomogeneous surface chemistry. The observed in Raman spectra weak signals at 592 and 1060 cm^{-1} have been previously attributed to MgO activated by Li-doping in the literature [42]. The weak signal of soluble aluminates ($[Al(OH)_4]^-$) and $MgCl_2$ were also observed, possibly originated from aluminates and $MgCl_2$ trapped in the precipitated brucite. The spatial expansion of both, $LiAlCO_3 \cdot H_2O$ (Li-Al-LDH) and brucite was consistent with the areas of cathodic hydrogen evolution (**Fig. 1a**), which may result from a local pH increase caused by the water reduction. It is noted that Li-Al-LDH was not detected outside of so-called cathodic zones.

The average growth rate of the $Mg(OH)_2$ (relative thickness increases with time) for zones of Type 1 and 2 is illustrated in **Fig. 1b.** This kinetics was assessed from the evolution of the in-situ measured 3652 cm^{-1} peak area in a given point (normalised by the water signal, visible as a large duplet around 3200-3400 cm^{-1}). The $Mg(OH)_2$ thickness increases much quicker on the points belonging to the Type 2 zones than on the points belonging to the Type 1 zones. Previously, significantly slower growth was communicated for the in-situ brucite growth on Mg in strongly alkaline solutions (pH>12.5) compared to Mg corroding in slightly alkaline conditions (pH 9-10.5) [27]. The in-situ Raman fingerprint of $Mg(OH)_2$ was also very different for the areas

of Type 1 (**Fig. 1c**) and Type 2 (**Fig. 1d**). The shape of the Raman peaks obtained on Type 1 areas was previously associated with thin films of brucite growing on pure Mg in strongly alkaline solutions; while Raman spectrum obtained from Type 2 area is similar to the Raman spectra representing the well-developed micrometric crystals formed by dissolution-re-precipitation from the solution at pH around 10 [27].

Corrosion products (including commonly reported carbonates) beyond those listed in **Table 1** were not detected by in-situ CRM in 0.1 M NaCl (Appendix 1, Fig. S2). Additional in-situ experiments in solution containing 0.1 M Na_2CO_3 for 2 hours (Appendix 1, Fig. S3) also did not result in the measurable formation of other corrosion products. Once the solution was removed from the cell and the ambient air entered in the contact with the sample for several hours, an obvious Li_2CO_3 Raman fingerprint indicated the formation of Li_2CO_3 **(Fig. 2**), which corroborates with the rapid formation of a Li_2CO_3 film upon Mg-Li(-Al-Y-Zr), when exposed to the air. This detection of the air-formed Li_2CO_3 gradually diminishes following re-immersion into NaCl solution (**Fig. 2),** indicating its possible dissolution which is coherent with relatively high solubility of Li_2CO_3 in water (8-13 g l^{-1}).

3.2. Chemical composition of the film from Nano Auger Electron Spectroscopy and Glow Discharge Optical Emission Spectroscopy

3.2.1. GD-OES analysis

Qualitative GD-OES elemental depth profiles obtained from the Mg-Li(-Al-Y-Zr) samples immediately after immersion in 0.1 M NaCl are shown in **Fig. 3a**. The surface film may be traced via the O signal in the depth profile. It was observed that the surface film immediately after immersion was mainly composed of Mg, C and O. Signals from Li were only be observed at the 'bottom' of the surface film immediately after immersion. From the GD-OES profiles of the same sample re-analysed after 3 hours of the contact with ambient air (**Fig. 3b**), Li enrichment accompanied by the increased C and O content at the outer layers of the surface film was evident, which again corroborates the ready formation of Li_2CO_3 and possibly the Mg carbonate/hydroxycarbonate during air-exposure. Such a tendency was reproducible for different immersion and air-exposure times and consistent with the in-situ Raman observations of rapid Li_2CO_3 formation during air-exposure of the preliminary immersed samples. A notable Li depletion in the metallic matrix in the direct vicinity of the oxidised surface (**Fig. 3**) was also observed.

The total eroded depth in GD-OES experiments was ~1.6 µm. While the metallic sputtering can be calibrated

in the eroded depth, the upper oxide thickness was estimated to be less than ~200 nm. For such a thin layer, the in-situ differential interferometry profiling (DiP) with the red laser ($\lambda \approx 600$ nm) was unable to describe exact depth evolution in the oxide layer (200 nm < $\lambda/2 \approx 300$ nm). Similarly, for the unknown and complex composition of corrosion products upon Mg-Li alloys, no calibration of the erosion rate could be made. For this reason, the evolution of the chemical composition was presented as a function of sputtering time.

3.2.2. AES analysis

Localised AES spectra and nano-AES profiles calculated from the AES spectra obtained on different locations of Type 1 "intact" Mg-Li matrix after 2 hours of immersion are shown in **Fig. 4 (a-d).** While only some representative spectra at different depth are shown in the spectral windows, the depth profile was generated using the totality of the data obtained from the spectra collected at 56 depth points. No Al, Y or Zr signal was detected on Mg-Li matrix and hence, the Y/Zr windows are not shown. In contrast, the Li (**Fig. 4 a**), Mg (**Figs. 4 a and 4 b**) and O (**Fig. 4 c**) are clearly detected and C (**Fig. 4 d**) was absent through the full depth of the film but was present on the outer-most surface before sputtering (the depth increase is indicated by the arrows "sputtering" in the figures). For comparison, the spectrum of pure Mg corroded in similar conditions (marked as reference in **Fig. 4**) is shown by dash lines. Indexes ^{a} or ^{b} for Mg identify if the fractions were calculated using the low energy region for Mg shown in **Fig. 4 a** or the high energy region for Mg shown in **Fig. 4 b**.

Although Auger spectroscopy is not commonly used to distinguish the oxidation state of metals, **Fig. 4 a** does none-the-less illustrate that only Li^+ and no metallic Li is present throughout the film thickness (KLL lines at 52.3 and 46.5 eV are expected for metallic Li, but 40.7 and 34.3 eV for Li^+ [43, 44]). Target factor analysis (TFA) was necessary to take into account possible interferences between Mg and Li^+ [45], and verify the number of the present species. The calculated depth profiles (**Fig. 4 e**), support the presence of Li^+, which is evidenced by the difference between the contribution of Mg (Mg^{b}_{ox} calculated from the spectra illustrated in window **Fig. 4 b**) and the experimentally obtained peak areas (Mg^{a}_{ox}+Li, calculated from the window shown in **Fig. 4 a**). For the thicknesses between 10 and 100 nm, a clear positive difference [At.%(Mg^{a}_{ox}+Li) – At.%(Mg^{b}_{ox})] confirms the presence of Li^+. The depletion of the alloy by Li^0 at the metal/oxide interface (**Fig. 4 e**) is consistent with the results of GD-OES.

The AES spectra of Mg and O (**Fig. 4 a-c**) confirmed the presence of two main components in Mg and O windows. The components of Mg signal, according to the literature [46, 47], were attributed to metallic Mg (peaks at 1186 eV and 1175.2 eV) and MgO (1180.6 eV). For O, the peak position is between the stoichiometric and oxygen deficient oxides, which suggests the presence of the defects or Li-doping [48] (peak

at 509.5-509.8 eV for Li_2O [43], and between 500 and 510 eV for MgO with different Mg/O ratios [48]). Previously, when considering different oxide stoichiometry, lower kinetic energy of oxygen was attributed to stronger oxidation (500 eV for stoichiometric MgO crystal). Hence, a relatively high value of kinetic energy of O peak is in favour of Mg deficient oxide, which is coherent with the oxide doped by Li^+.

Notably, the presence of $Mg(OH)_2$ is not evident on the AES results obtained from the Mg-Li(-Al-Y-Zr) sample when comparing to the spectra of $Mg(OH)_2$ formed on pure Mg immersed in similar conditions (dash lines in **Fig. 4 b-c**). The absence of $Mg(OH)_2$ might be attributed to the rapid CO_2 adsorption which transformed the thin in-situ formed $Mg(OH)_2$ into Mg hydroxycarbonates. Since the C signals was only detected at the outer most part of the surface (the first spectrum in **Fig. 4 d**), its thickness is below 8 nm *(as calibrated by the erosion depth of SiO_2 sputtered in similar conditions). Considering that the density of Mg carbonates varies from 0.8 (hydromagnesite) to 1.5 (magnesite) times from the density of $Mg(OH)_2$, one can suppose that the $Mg(OH)_2$ thickness before its carbonation is in the same order of magnitude as the thickness of Mg carbonates, hence far below than 10 nm (in equivalent SiO_2 thickness)..* The in-situ formed $Mg(OH)_2$ (thus the transformed Mg carbonates) is proposed to be several nm thick in the tested area.

The qualitative AES depth profiles obtained for a small Y-containing particle situated in the "intact" anodic zone demonstrated the presence of less than 10 nm Li, C and O rich film (Appendix 2, Fig. S4). This Y-containing particle also showed significantly slower erosion rate than the surrounding matrix.

3.3. Selective dissolution during aqueous exposure

To monitor the continuous evolution of the surface chemistry on the Mg-Li(-Al-Y-Zr) alloy during immersion, the stoichiometry of the ion release from a freshly ground Mg-Li(-Al-Y-Zr) sample was monitored using AESEC in 0.01M NaCl (**Fig. 5 a**). Following initial contact of the surface with the solution, dissolution of Li in excess of the alloy stoichiometry was observed, which indicated the Li was selectively dissolved when the fresh Mg-Li surface in contact with aqueous test solution. Similar preferred dissolution of Li was also reported in a previous research [16] where an excessive dissolution event happened after the surface of a Mg-Li(-Al-Y-Zr) alloy was scratched in-situ. After the initial abrupt dissolution, the measured Li dissolution rate decreased rapidly, reaching a relatively stable value after ~150 seconds of immersion. At this point (150 seconds of immersion), the ratio between the release rates of Mg^{2+} and Li^+ (Mg : Li) reached ~2, correlating well with the bulk composition of the alloy. Afterwards, the dissolution rate of Mg decreased consistantly while the dissolution rate of Li stayed constant. The fraction of soluble Mg^{2+} is smaller than expected from the stoichiometry of the alloy (**Table 2**), indicating the formation of a Mg-rich surface film that is coherent

with the observation of GD-OES in previous sections.

The potentiostatic anodic polarisation (+200 mV vs Open Circuit Potential) following 2000 seconds at OCP, further enhanced the selective Li dissolution (**Fig. 5**). The minor increase of Mg dissolution rate at the beginning of polarisation could be attributed to the dissolution of Mg-rich film formed during the OCP exposure. Notably, after polarisation for a brief period (~ 500 s), the Mg dissolution rate decreased again but this decrease was not accompagnied by the decrease of the total current. One can note, that during intitial 500 s anodic polarization the difference between the total current measured by the potentiostate and the summ of the dissolution rates of Mg^{2+} and Li^{+}, re-calculated as currents using Faraday's law, was less than 5 %. This indicated that AESEC measured mainly Faradaic dissolution in the first 500 s of polarization.

As measured by AESEC, stoichiometric dissolution and selective dissolution of Li during short immersions and short polarisation of freshly polished Mg-Li(Al-Y-Zr) was not identical with the observations of Hou et al. [15]. To understand this, it is important to take into account the difference in the flow condition and cell design. In our experiments, different cell geometry (co-axial flow parrallel to the sample surface) and much higher flow rate were used; this results in more rapid and voluminous extraction of ions from the surface, and hence slower film formation, which could rationalise the observed differences between the obtained data.

In an attempt to characterise the surface chemistry of the film formed after relatively long aqueous immersion, the ion release was monitored in 0.01 M NaCl aqueous solution on a Mg-Li(-Al-Y-Zr) surface after 20 hours of preliminary immersion. The AESEC analysis of the immersed sample showed an apparent higher dissolution rate of Mg than Li, even though the dissolution of both Mg and Li were strongly decreased (Fig. 5b). However, in the solution used for long immersion, the fraction of dissolved Li^{+} in the solution was higher than the fraction expected from stoichiometry (**Table 2**); implying that a selective Li dissolution happened during the ealier stages of the immersion. The measured higher dissolution rate of Mg after 20 hours of immersion might be hence due to the residual surface, already depleted by Li.

The composition of the film formed after 20 hours of immersion was further verified by monitoring of the particles detached from the film after a surface scratch was applied during the AESEC experiment. The monitoring was stopped for 30 seconds, the surface of the tested sample was scratched by a sapphire lancet, then the experiment was resumed. In previous research, it has been observed that particles present in the solution appears as spikes on the AESEC dissolution curve [35, 49]. From the elemental dissolution profiles in **Fig. 5 b,** it can be seen that many spikes appeared on the Mg dissolution curve after the sample surface was scratched. Therefore, these particles may be proposed to be insoluble Mg-rich fragments of the surface film

peeled off by the electrolyte flow near the scratched site. The observation of Mg-rich fragments released from the surface further corroborated the formation of a Mg-rich surface film.

3.4. The influence of soluble Li^+ to the surface film formed on pure Mg during aqueous exposure

In previous sections, AESEC results indicated the formation of a Mg-rich surface film in aqueous environment while the in-situ CRM and ex-situ AES indicated that the presence of modified (Li-doped) MgO. In order to observe the influence of soluble Li^+ to the Mg-rich surface film on Mg alloys, the surface films formed on pure Mg samples (50 ppm Fe) in 0.1M NaCl and in 0.1 M LiCl were characterised with initial pH adjusted between 8.6 and 8.9 (4 ml of solution, exposed surface of 0.78 cm^2).

The initial solution conductivity was measured as 8.3 mS for NaCl and 4.3 mS for LiCl, indicating potentially more rapid charge transfer in Na^+-rich electrolyte than in Li^+-rich electrolyte. After 1 hour of immersion, in 4 ml of solution, it was noted that the surface immersed in LiCl was much more homogenous, exhibiting no filaments. Raman spectra (not shown) did not reveal the difference in the peak positions between the samples immersed in the two solutions. However, the intensities of both brucite peaks (444 cm^{-1} and 3652 cm^{-1}) were significantly higher for the sample immersed in NaCl than in LiCl solutions, indicating a higher rate of brucite formation in the former aqueous environment. GD-OES elemental depth profiles of the two samples (Appendix 3, Fig. S5) demonstrated that Li or Na are present through the oxide layer, indicating that both of the ions may participate in doping of MgO and could hence compete for doping during aqueous corrosion of Mg-Li alloys. Notably, the erosion time necessary to reach the alloy substrate for the sample immersed in LiCl was nearly 5 times longer than that of sample immersed in NaCl, which could specify either thicker or more compact and less conductive film formed in LiCl solution.

Photoluminescence spectroscopy of the formed films demonstrated the presence of uncharged oxygen vacancies (F^{2+} centres, "2+" charged oxygen vacancies, $V_O^{\bullet\bullet}$ in Kröger–Vink notation) typical for MgO in both the samples (the spectra being similar in the high energy region, this region is not shown). Clear differences in photoluminescence spectra were detected in the region between 2 and 4 eV as illustrated in **Fig. 6.**

Under UV excitation, the oxide formed in NaCl showed a very weak and broad photoluminescence signal at 2.3 eV, which usually associated with the presence of F^0-centers in undoped MgO [50, 51]. Similar, but more

intense, photoluminescence signal was observed in the dark cathodic zone (point "1" in **Fig. 6 a)** on the sample immersed in LiCl while the signal on the brilliant (point "3") and light grey areas (point "2") demonstrated not only this emission but also a strong orange photoluminescence signal above 2.8 eV. The strong orangephotoluminescence was previously associated with stabilization of F^+ centres in Li-doped MgO [39] and not with Li_2O inclusions which was demonstrated via long time stability of the signal in humid atmosphere despite high hygroscopicity of Li_2O. The photoluminescence signal of F^+ centres in the undoped MgO is expected at 2.7 eV while Li doping was reported to shift it up to 2.9 eV [51]. The photoluminescence spectra demonstrated that the presence of soluble Li^+ is sufficient to modify the electronic structure (and hence the chemical reactivity) of MgO, increasing the stability of the oxygen vacancies with trapped electrons (F^+-centres). Lower conductivity of the LiCl solutions compared to the NaCl solution with same molar concentration can be another reason of a lower reactivity at the interface if the dissolved Li^+ ions are trapped in the oxide-hydroxide film. The effect of soluble Li^+ on the corrosion mechanisms of Mg-Li alloy will be discussed in the next section.

Discussion

4.1. The in-situ surface evolution of Mg-Li(-Al-Y-Zr)

It is now well known, that the surface films formed upon Mg-alloys (in general) exhibits a layered structure, comprised by a combination of oxide, hydroxides and carbonates with thicknesses ranging from few nanometres to several tens of micrometres; depending on the exposure condition and the alloy composition [52-55]. The development of such surface films that span numerous length scales also implies the need to employ a wide range of analytical tools with various capabilities.

As shown in the results section, the surface film formed on the Mg-Li (Al-Y-Zr) alloy in aqueous solution was observed to be mainly composed of Mg corrosion products. On the anodic zones, a relatively thick (~90 nm thick after 2 h of immersion) (Li-doped) MgO film covered the Li-depleted metallic Mg-Li matrix. The external hydrated layer, detected by the in-situ CRM on these zones, was observed to be relatively thin (when compared with pure Mg in similar conditions). The slow growth kinetics of the hydrated layer as well as its in-situ Raman fingerprint are very similar to the thin and compact brucite films formed on pure Mg at pH>12.5 [27].

The mechanisms of the surface film formation during initial aqueous exposure of the Mg-Li(-Al-Y-Zr) alloy, evidenced by our work, is schematically presented in **Fig. 7.** At the beginning of immersion, Li is selectively

dissolved in aqueous corrosion (step 1). Then a non-stoichiometric MgO film with an excess of Mg^{2+} grows in-situ (step 2). The soluble Li^+ can replace Mg^{2+} in the in-situ formed MgO film and becomes a dopant in the in-situ formed film (step 3) as well as participate in the local LDH build up (step 4). Near cathodic areas, Li^+ can additionally participate in the localized formation of Li-Al LDH (step 4). Both, soluble Li^+ and Li^+ incorporated in the MgO could further modify the aqueous stability of the substrate.

4.2. The effect of Li^+ on the aqueous stability of Mg-Li alloys

For the most of Mg alloys the corrosion rate increases with the immersion time (more specifically, with increasing anodic dissolution) owing to the "cathodic activation" effect, which is attributed to the growth of the effective volume of the cathode on the surface, also aided by the transformation of anodic sites to cathodic sites [56-59]. However, this effect seems not to occur for the studied Mg-Li(-Al-Y-Zr) alloy, as revealed by the AESEC test, in which the corrosion rate decreased with OCP exposure (and with anodic polarisation), indicating a possible modification of the corrosion mechanism.

In previous works, the formation of certain carbonates upon cathode sites was proposed to be able to increase the corrosion resistance by inhibiting the cathodic reaction of corrosion [60]. More specifically, Al-Li LDH ($Li_2[Al_2(OH)_6]_2{\cdot}CO_3{\cdot}nH_2O$) was considered as a possible protective film [13, 61-64]. In-situ CRM demonstrated that the Al-Li LDH developed gradually near the cathodic sites of the Mg-Li(-Al-Y-Zr) sample. Therefore, it can be speculated that the gradual development of $Li_2[Al_2(OH)_6]_2{\cdot}CO_3{\cdot}nH_2O$ on cathodic areas could arrest their expansion with time and prevent "cathodic activation". Nevertheless, at the time scales studied in this work, the hydrogen evolution on these sites did not show any remarkable inhibition and the present work cannot confirm nor decline such a hypothesis. The contribution of Li-Al LDH to the corrosion resistance of Mg-Li(-Al-Y-Zr) alloys still needs further research.

The modification of magnesium oxide/hydroxide film by Li-incorporation can be also considered because no other lithium containing compound forming a continuous surface film in aqueous condition was detected on the studied alloy. The formation of the oxide/hydroxide film during aqueous corrosion of Mg could undergo several transformation mechanisms. Low electrochemical potential of Mg results in its spontaneous oxidation (reaction 1) and hydrogen reduction (reaction 2) in contact with aqueous solutions [65]:

$$Mg \rightarrow Mg^{2+} + 2e^- \quad (1)$$

$$2H_2O + 2e^- \rightarrow H_2 + 2OH^- \quad (2)$$

A stoichiometric and compact MgO film could efficiently limit mass or charge transfer and inhibit corrosion.

However, the naturally formed MgO on Mg and its alloys contains numerous defects and is, by consequence, highly reactive in the presence of water, showing a tendency of rapid hydration, dissolution and transformation into $Mg(OH)_2$ via the dissolution-precipitation process [66]:

$$MgO+H_2O \rightarrow Mg\text{-}O\cdots HOH \rightarrow Mg^{2+}_{aq} + 2\ OH^- \leftrightarrows Mg(OH)_2 \quad (3)$$

The resultant $Mg(OH)_2$ film was proposed to be compact and stable at strongly alkaline pH [27, 67, 68], however the porous and continuously evolving oxide-hydroxide film formed in neutral and slightly alkaline conditions [66] is unable to protect Mg alloys [69]. Therefore, the MgO aqueous stability in initially neutral solutions could be one of the critical issues affecting Mg corrosion. MgO hydration and dissolution occur via high energy charged surfaces and defect sites [70-75] and the activity in these processes can be considered as a charge compensation via different processes schematically presented in **Fig. 8a**. *In the figure as well as in reaction schemas below, Kröger–Vink notation is used. Namely, uncharged oxygen vacancies with 2 trapped electrons, or F-centers, appear as $[V_O]$; oxygen vacancies with one trapped electron, F^+ centers, appear as $[V_O^{\bullet}]$; double charged oxygen vacancies without trapped electrons, F^{2+} centers, are noted as $[V_O^{\bullet\bullet}]$.* The ionisation potential and the electron affinity of different clusters containing Mg^{2+}, O^{2-} and oxygen vacancies indicate if these sites will act as electron donors or rather behave as electron acceptors; and hence determine if the corrosion product film will support cathodic hydrogen reduction [76].

According to the AESEC results, mobile Li^+ ions could be rapidly available at the metal/solution interface by the preferred electrochemical dissolution during aqueous corrosion of freshly Mg-Li surface (reaction 4a) or at the first moments via hydrolysis of the accumulated during air exposure Li_2CO_3 (reaction 4b):

$$Li \rightarrow Li^+_{aq} + e^- \quad (4a)$$

$$Li_2CO_3\ H_2O \rightarrow 2Li^+_{aq} + HCO_3^- + OH^- \quad (4b)$$

A potential impact of the reaction 4b can be illustrated considering $pK_a(HCO_3^-)=10.33$. For example, in 10^{-2} M Li_2CO_3 electrolyte, the expected solution pH (11.16) is higher than the pH of about 10, usually measured during corrosion of pure Mg in initially neutral NaCl solutions. The dissolved Li^+ could be easily incorporated in the MgO film, as demonstrated by photoluminiscence spectroscopy and GD-OES, and helps to stabilizing the F-centres and charge compensation (process 5 in Fig. 8) as schematically illustrated below:

$$[V_O^{\bullet\bullet}] + 2\ Li^+ \leftrightarrows [Li_{Mg}^{'}\text{-}V_O^{\bullet\bullet}\text{-}Li_{Mg}^{'}]^x \quad (5)$$

$$[V_O^{\bullet}] + Li^+ \leftrightarrows [Li_{Mg}^{'}\text{-}V_O^{\bullet}]^x \quad (6)$$

Thus, the charge compensation by Li^+ incorporation schematically presented in **Fig. 8b** can reduce other charge compensation mechanisms (processes 1-4 in **Fig. 8 a**), which are responsible for dissolution, structural

modification and support of cathodic reactivity. The stabilization of F^+ centres in the presence of Li^+ ions was also supported by photoluminescence spectra.

Owing to the close ionic radii of Mg^{2+} (79 pm) and Li^+ (78 pm), the mechanical integrity of the MgO film should not be affected much by Li^+ doping. However, the charge of Li^+ is only half of the charge of Mg^{2+}, which significantly reduces the Li^+ affinity to the surrounding water and its tendency for hydration compared to Mg^{2+}. It may be expected that the decrease of the surface charge by replacing Mg^{2+} by Li^+ on Mg-terminated <111> surfaces of MgO can significantly slow the hydration rate of these surfaces with high surface energy [8], which are most susceptible to hydration [72, 73]. Such an interpretation is coherent with the observed slow brucite growth (in-situ Raman spectroscopy and nano-AES), which is significantly slower than reported on pure Mg in similar conditions [27]. The lower erosion rate of the oxide film containing Li during GD-OES is also coherent with previously reported sever sintering of MgO in the presence of Li^+. Since the hydration of MgO is dependent on the crystal size, the MgO sintering can also contribute to the reduction of hydration rate [77, 78].

Considering the catalytic cathodic activity of the oxide-hydroxide film, recent quantum mechanics calculations suggested that Li-doped MgO have higher ionization energy and lower electron affinity than undoped MgO [76], which supports the hypothesis of a less pronounced catalytic cathodic water reduction on Li-doped MgO. The latter is also coherent with the known high activity of Li-doped MgO in oxidative coupling reaction of methane CH_4 [23].

Therefore, it can be proposed that the local concentration of dissolved Li^+ at the metal – NaCl solution interface decreases the local conductivity, while hydrolysis of Li_2CO_3 (reaction 4b) leads to a rapid increase of the local pH, coherent with the features observed by in-situ CRM.

4.3. The effect of Li content in the alloy on the metal / oxide interface stability

The previously proposed schema considers the benefits of Li^+ on aqueous stability of Mg but is insufficient to explain the critical Li concentration in the alloy observed in the literature, below which the alloy stays unprotected. Li et al. [79] previously considered a Pilling Bedworth ratio (PBR, defined as the ratio between the molar volumes of the oxide and the metal [80]), to explain the protective nature of Li_2CO_3 film on Mg-Li alloys but were not able to explain the effect of the Li content in the alloy for this film. In the case of Mg-Li alloys with the surface film chemistry detected in-situ in our work, the PBR (**Fig. 9**) was also calculated using equations (7-9) considering the formation of a cubic Li-doped MgO film:

$$PBR(MgO/MgLi) = \frac{M(MgO)\cdot\rho(MgLi)}{n\cdot\rho(MgO)\cdot M(MgLi)} = 0.8 \ \ (<1) \quad (7)$$

$$M(MgLi) = \frac{at\%(Mg)\cdot M(Mg)+at\%(Li)\cdot M(Li)}{100\ \ \%} \quad (8)$$

$$n = \frac{at\%(Mg)}{100\ \ \%} \quad (9)$$

where *M(MgLi)* and *M(MgO)* denote molar masses of Mg-Li alloy and MgO; the at %(Li) and at %(Mg) are Li and Mg contents in the alloy; *n* takes into account that only Mg (and not Li) atoms participate in the formation of MgO. The oxide density *ρ(MgO)* was considered constant for low doping levels. The alloy density ρ(MgLi), which dependent on the Li-content, was taken from the literature [81].

The results shown in Fig. 9 clearly demonstrate that the condition of a protective film (PBR>1) requires a minimal Li concentration in the alloy close to 15-18 at. %. Thus, replacing the in-situ detected surface film composition, our speculative model is able to explain the effect of Li content in the alloy on the aqueous stability of Mg-Li alloys.

Conclusions

The combination of in-situ surface and solution analysis during aqueous exposure of a bcc Mg-Li(-Al-Y-Zr) alloy was corroborated by ex-situ photoluminescence measurement, GD-OES nano-AES. The present study was able to explore and advance the understanding related to the role of Li on reactivity of the Mg-Li(Al-Y-Zr) alloy.

It was determined, based on the techniques employed, that the in-situ developed film upon Mg-Li(Al-Y-Zr) alloy consisted of a Li-doped MgO on a Li-depleted metallic matrix. The $Mg(OH)_2$ at the outer surface of the film was approximately ten times thinner than that of the MgO present. *More precisely, according to the ex-situ AES depth profiles, the oxide layer was about 90 nm thick, while the $Mg(OH)_2$ thickness, estimated from the quantity of Mg carbonates at the extreme surface, was less than 10 nm.* The kinetics of brucite ($Mg(OH)_2$) formation was slow when compared to $Mg(OH)_2$ growth on unalloyed Mg (or Li-free hcp Mg-alloys) in similar conditions. Compounds containing Al and Y were formed locally in vicinity of cathodic sites, in particular for the first time the formation and expansion of Li-Al LDH ($Li_2[Al_2(OH)_6]_2\cdot CO_3\cdot nH_2O$) around cathodic areas was identified in-situ upon Mg-Li(-Al-Y-Zr) immersed in flowing 0.1 M NaCl.

A possible mechanism of corrosion protection has been speculated, which is able to rationalise the experimentally observed slow brucite growth, stability and compactness of MgO and the in-situ aqueous

stability of the studied alloy. In addition, the work herein was able to elaborate the critical role of Li and Li content in Mg-Li alloys for aqueous stability. The stability of the alloy was postulated to arise from several complementary processes. Firstly, mobile soluble Li^+, which could be released by the electrochemical dissolution of the alloy or from the accumulated air-formed Li-rich corrosion products may replace Mg^{2+} in naturally formed MgO, contributing to the charge compensation of the polar surfaces and point defects. This would increase the chemical stability of the surface film / oxide. Additionally, inhibition of so-called cathodic activation is anticipated from stabilization of Li-doped MgO, and from the in-situ detected Li-Al LDH upon cathodic areas.

Acknowledgements

The authors acknowledge the Embassy of France in Australia for the Nicolas Baudin travel grant of Y. Yan.

References

[1] Z. Zeng, N. Stanford, C.H.J. Davies, J.-F. Nie, N. Birbilis, Magnesium extrusion alloys: a review of developments and prospects, International Materials Reviews, 64 (2019) 27-62.
[2] H. Haferkamp, R. Boehm, U. Holzkamp, C. Jaschik, V. Kaese, M. Niemeyer, Alloy development, processing and applications in magnesium lithium alloys, Materials Transactions, 42 (2001) 1160-1166.
[3] R. Ninomiya, K. Miyake, A study of superlight and superplastic Mg-Li based alloys, Journal of Japan Institute of Light Metals, 51 (2001) 509-513.
[4] G.H. Park, J.T. Kim, H.J. Park, Y.S. Kim, H.J. Jeong, N. Lee, Y. Seo, J.-Y. Suh, H.-T. Son, W.-M. Wang, J.M. Park, K.B. Kim, Development of lightweight MgLiAl alloys with high specific strength, Journal of Alloys and Compounds, 680 (2016) 116-120.
[5] H. Zhong, L. Feng, P. Liu, T. Zhou, Design of a Mg-Li-Al-Zn alloy by means of CALPHAD approach, Journal of Computer-Aided Materials Design, 10 (2005) 191-199.
[6] Y. Tang, Q. Le, W. Jia, L. Fu, X. Liu, J. Cui, Microstructure evolution and strengthening mechanism study of Mg-Li alloys during deformation and heat treatment, Materials Science and Engineering: A, 704 (2017) 344-359.
[7] R. Li, B. Jiang, Z. Chen, F. Pan, Z. Gao, Microstructure and mechanical properties of Mg14Li1Al0.3La alloys produced by two-pass extrusion, Journal of Rare Earths, 35 (2017) 1268-1272.
[8] J. Zhao, J. Zhang, W. Liu, G. Wu, L. Zhang, Effect of Y content on microstructure and mechanical properties of as-cast Mg–8Li–3Al–2Zn alloy with duplex structure, Materials Science and Engineering: A, 650 (2016) 240-247.
[9] W. Xu, N. Birbilis, G. Sha, Y. Wang, J.E. Daniels, Y. Xiao, M. Ferry, A high-specific-strength and corrosion-resistant magnesium alloy, Nature Materials, 14 (2015) 1229-1235.
[10] D.S. Gandel, M.A. Easton, M. Gibson, N. Birbilis, Influence of Mn and Zr on the corrosion of Al-free Mg alloys: Part 2 - Impact of Mn and Zr on Mg alloy electrochemistry and corrosion, Corrosion, 69 (2013) 744-751.
[11] S. Tang, T. Xin, W. Xu, D. Miskovic, G. Sha, Z. Quadir, S. Ringer, K. Nomoto, N. Birbilis, M. Ferry, Precipitation strengthening in an ultralight magnesium alloy, Nature Communications, 10 (2019) 1003.
[12] S. Kamado, Y. Kojima, Deformability and strengthening of superlight Mg-Li alloys, Metallurgical science and technology, 16 (1998) 45-54.
[13] Y.M. Yan, O. Gharbi, A. Maltseva, X.B. Chen, Z.R. Zeng, S.W. Xu, W.Q. Xu, P. Volovich, M. Ferry, N. Birbilis, Investigating the Structure of the Surface Film on a Corrosion Resistant Mg-Li(-Al-Y-Zr) Alloy, Corrosion, 75 (2019) 80-89.

[14] R.C. Zeng, L. Sun, Y.F. Zheng, H.Z. Cui, E.H. Han, Corrosion and characterisation of dual phase Mg-Li-Ca alloy in Hank's solution: The influence of microstructural features, Corrosion Science, 79 (2014) 69-82.
[15] L. Hou, M. Raveggi, X.-B. Chen, W. Xu, K.J. Laws, Y. Wei, M. Ferry, N. Birbilis, Investigating the Passivity and Dissolution of a Corrosion Resistant Mg-33at.%Li Alloy in Aqueous Chloride Using Online ICP-MS, Journal of The Electrochemical Society, 163 (2016) C324-C329.
[16] Y. Yan, P. Zhou, O. Gharbi, Z. Zeng, X. Chen, P. Volovitch, K. Ogle, N. Birbilis, Investigating ion release using inline ICP during in situ scratch testing of an Mg-Li(-Al-Y-Zr) alloy, Electrochemistry Communications, 99 (2019) 46-50.
[17] Y. Song, D. Shan, R. Chen, E.H. Han, Investigation of surface oxide film on magnesium lithium alloy, Journal of Alloys and Compounds, 484 (2009) 585-590.
[18] Z.-Y. Ding, L.-Y. Cui, R.-C. Zeng, Y.-B. Zhao, S.-K. Guan, D.-K. Xu, C.-G. Lin, Exfoliation corrosion of extruded Mg-Li-Ca alloy, Journal of Materials Science & Technology, 34 (2018) 1550-1557.
[19] Z. Chen, C. Bao, G. Wu, Y. Jian, L. Zhang, Effect of YAl2 Particles on the Corrosion Behavior of Mg–Li Matrix Composite in NaCl Solution, Materials, 12 (2019) 549.
[20] H.R. Eisenberg, R. Baer, Exothermic Mechanism for the Abstraction of Hydrogen from Methane on Li-Doped MgO, The Journal of Physical Chemistry C, 119 (2015) 196-215.
[21] I. Balint, K.-i. Aika, Specific defect sites creation by doping MgO with lithium and titanium, APPL SURF SCI, 173 (2001) 296-306.
[22] G.H. Dai, Q.J. Yan, Y. Wang, Q.S. Liu, Li-doped MgO as catalysts for oxidative coupling of methane: A positron annihilation study, Chemical Physics, 155 (1991) 275-284.
[23] M. Anpo, Y. Yamada, T. Doi, I. Matsuura, S. Coluccia, A. Zecchina, M. Che, Photoluminescence, Photo-Induced Reactivities and Catalytic Properties of Na- and Li-Doped Mgo, in: C. Morterra, A. Zecchina, G. Costa (Eds.) Studies in Surface Science and Catalysis, Elsevier, 1989, pp. 1-10.
[24] O. Myagmarjav, J. Ryu, Y. Kato, Lithium bromide-mediated reaction performance enhancement of a chemical heat-storage material for magnesium oxide/water chemical heat pumps, Applied Thermal Engineering, 63 (2014) 170-176.
[25] H. Ishitobi, N. Hirao, J. Ryu, Y. Kato, Evaluation of Heat Output Densities of Lithium Chloride-Modified Magnesium Hydroxide for Thermochemical Energy Storage, Industrial & Engineering Chemistry Research, 52 (2013) 5321-5325.
[26] C. Chen, C. Wu, Y. Chen, J. Niu, Effect of boric acid and lithium chloride on magnesium oxysulfate cement, IOP Conference Series: Earth and Environmental Science, 186 (2018) 012064.
[27] A. Maltseva, V. Shkirskiy, G. Lefèvre, P. Volovitch, Effect of pH on Mg(OH)2 film evolution on corroding Mg by in situ kinetic Raman mapping (KRM), Corrosion Science, 153 (2019) 272-282.
[28] N. Furuya, A. Matsuyuki, S. Higuchi, S. Tanaka, Determination of nitrate ion in waste and treated waters by laser raman spectrometry, Water Research, 13 (1979) 371-374.
[29] K.M. Cunningham, M.C. Goldberg, E.R. Weiner, Investigation of detection limits for solutes in water measured by laser Raman spectrometry, Analytical Chemistry, 49 (1977) 70-75.
[30] P. Vandenabeele, J. Jehlička, P. Vítek, H.G.M. Edwards, On the definition of Raman spectroscopic detection limits for the analysis of biomarkers in solid matrices, Planetary and Space Science, 62 (2012) 48-54.
[31] K. Kneipp, H. Kneipp, I. Itzkan, R.R. Dasari, M.S. Feld, Ultrasensitive Chemical Analysis by Raman Spectroscopy, Chemical Reviews, 99 (1999) 2957-2976.
[32] K. Ogle, Atomic Emission Spectroelectrochemistry: A new look at the corrosion, dissolution & passivation of complex materials, Corrosion and Materials, 37 (2012) 58-65.
[33] P. Zhou, M.J. Hutchison, J.R. Scully, K. Ogle, The anodic dissolution of copper alloys: Pure copper in synthetic tap water, Electrochimica Acta, 191 (2016) 548-557.
[34] K. Ogle, M. Serdechnova, M. Mokaddem, P. Volovitch, The cathodic dissolution of Al, Al2Cu, and Al alloys, Electrochimica Acta, 56 (2011) 1711-1718.
[35] M. Mokaddem, P. Volovitch, F. Rechou, R. Oltra, K. Ogle, The anodic and cathodic dissolution of Al and Al–Cu–Mg alloy, Electrochimica Acta, 55 (2010) 3779-3786.
[36] K. Ogle, M. Mokaddem, P. Volovitch, Atomic emission spectroelectrochemistry applied to dealloying phenomena II. Selective

dissolution of iron and chromium during active–passive cycles of an austenitic stainless steel, Electrochimica Acta, 55 (2010) 913-921.
[37] K. Ogle, J. Baeyens, J. Swiatowska, P. Volovitch, Atomic emission spectroelectrochemistry applied to dealloying phenomena: I. The formation and dissolution of residual copper films on stainless steel, Electrochimica Acta, 54 (2009) 5163-5170.
[38] B. Lafuente, R.T. Downs, H. Yang, N. Stone, The power of databases: The RRUFF project, in: T. Armbruster, R.M. Danisi (Eds.) Highlights in Mineralogical Crystallography, De Gruyter, Inc., Berlin, 2015.
[39] H. Soma, T. Uchino, Blue and Orange Photoluminescence and Surface Band-Gap Narrowing in Lithium-Doped MgO Microcrystals, The Journal of Physical Chemistry C, 121 (2017) 1884-1892.
[40] P.W. Palmberg, P.E. Industries, Handbook of Auger Electron Spectroscopy: A Reference Book of Standard Data for Identification and Interpretation of Auger Electron Spectroscopy Data, Physical Electronics Industries, 1972.
[41] M.L. Trudeau, Surface Chemistry and Microstructure Analysis of Novel Technological Materials, in: D.G. Rickerby, G. Valdrè, U. Valdrè (Eds.) Impact of Electron and Scanning Probe Microscopy on Materials Research, Springer Netherlands, Dordrecht, 1999, pp. 301-323.
[42] L. Escobar-Alarcón, T. Klimova, J. Escobar-Aguilar, S. Romero, C. Morales-Ramírez, D. Solís-Casados, Preparation and characterization of Al2O3–MgO catalytic supports modified with lithium, Fuel, 110 (2013) 278-285.
[43] C.F. Mallinson, J.E. Castle, J.F. Watts, Analysis of the Li KLL Auger Transition on Freshly Exposed Lithium and Lithium Surface Oxide by AES, Surface Science Spectra, 20 (2013) 113-127.
[44] N. Ishida, D. Fujita, Chemical-state imaging of Li using scanning Auger electron microscopy, Journal of Electron Spectroscopy and Related Phenomena, 186 (2013) 39-43.
[45] M.-C. Wu, C.M. Truong, D.W. Goodman, Electron-energy-loss-spectroscopy studies of thermally generated defects in pure and lithium-doped MgO(100) films on Mo(100), Physical Review B, 46 (1992) 12688-12694.
[46] I.J.T. Jensen, A. Thøgersen, O.M. Løvvik, H. Schreuders, B. Dam, S. Diplas, X-ray photoelectron spectroscopy investigation of magnetron sputtered Mg–Ti–H thin films, International Journal of Hydrogen Energy, 38 (2013) 10704-10715.
[47] O. Friedrichs, J.C. Sánchez-López, C. López-Cartes, M. Dornheim, T. Klassen, R. Bormann, A. Fernández, Chemical and microstructural study of the oxygen passivation behaviour of nanocrystalline Mg and MgH2, Applied Surface Science, 252 (2006) 2334-2345.
[48] A.P. Janssen, R.C. Schoonmaker, A. Chambers, M. Prutton, Low energy Auger and loss electron spectra from magnesium and its oxide, Surface Science, 45 (1974) 45-60.
[49] M. Serdechnova, P. Volovitch, K. Ogle, Atomic emission spectroelectrochemistry study of the degradation mechanism of model high-temperature paint containing sacrificial aluminum particles, Surface and Coatings Technology, 206 (2012) 2133-2139.
[50] W.C. Las, T.G. Stoebe TL Mechanisms and Luminescence Characteristics in MgO, Radiation Protection Dosimetry, 8 (1984) 45-67.
[51] G.H. Rosenblatt, M.W. Rowe, G.P. Williams, R.T. Williams, Y. Chen, Luminescence of F and F+ centers in magnesium oxide, Physical Review B, 39 (1989) 10309-10318.
[52] Z.P. Cano, J.R. McDermid, J.R. Kish, Cathodic Activity of Corrosion Filaments Formed on Mg Alloy AM30, Journal of The Electrochemical Society, 162 (2015) C732-C740.
[53] K.A. Unocic, H.H. Elsentriecy, M.P. Brady, H.M. Meyer, G.L. Song, M. Fayek, R.A. Meisner, B. Davis, Transmission Electron Microscopy Study of Aqueous Film Formation and Evolution on Magnesium Alloys, Journal of The Electrochemical Society, 161 (2014) C302-C311.
[54] M. Liu, S. Zanna, H. Ardelean, I. Frateur, P. Schmutz, G. Song, A. Atrens, P. Marcus, A first quantitative XPS study of the surface films formed, by exposure to water, on Mg and on the Mg–Al intermetallics: Al3Mg2 and Mg17Al12, CORROS SCI, 51 (2009) 1115-1127.
[55] R.C. Phillips, J.R. Kish, Nature of Surface Film on Matrix Phase of Mg Alloy AZ80 Formed in Water, CORROSION, 69 (2013) 813-820.
[56] S. Thomas, O. Gharbi, S.H. Salleh, P. Volovitch, K. Ogle, N. Birbilis, On the effect of Fe concentration on Mg dissolution and activation studied using atomic emission spectroelectrochemistry and scanning electrochemical microscopy, Electrochimica Acta, 210 (2016) 271-284.

[57] R.L. Liu, M.F. Hurley, A. Kvryan, G. Williams, J.R. Scully, N. Birbilis, Controlling the corrosion and cathodic activation of magnesium via microalloying additions of Ge, Scientific Reports, 6 (2016) 28747.
[58] S. Fajardo, G.S. Frankel, Effect of impurities on the enhanced catalytic activity for hydrogen evolution in high purity magnesium, Electrochimica Acta, 165 (2015) 255-267.
[59] N. Birbilis, A.D. King, S. Thomas, G.S. Frankel, J.R. Scully, Evidence for enhanced catalytic activity of magnesium arising from anodic dissolution, Electrochimica Acta, 132 (2014) 277-283.
[60] M. Esmaily, D.B. Blücher, J.E. Svensson, M. Halvarsson, L.G. Johansson, New insights into the corrosion of magnesium alloys — The role of aluminum, Scripta Materialia, 115 (2016) 91-95.
[61] O. Gharbi, N. Birbilis, K. Ogle, Li reactivity during the surface pretreatment of Al-Li alloy AA2050-T3, Electrochimica Acta, 243 (2017) 207-219.
[62] P. Visser, Y. Liu, H. Terryn, J.M.C. Mol, Lithium salts as leachable corrosion inhibitors and potential replacement for hexavalent chromium in organic coatings for the protection of aluminum alloys, Journal of Coatings Technology and Research, 13 (2016) 1-10.
[63] P. Visser, Y. Gonzalez-Garcia, J.M.C. Mol, H. Terryn, Mechanism of Passive Layer Formation on AA2024-T3 from Alkaline Lithium Carbonate Solutions in the Presence of Sodium Chloride, Journal of The Electrochemical Society, 165 (2018) C60-C70.
[64] R.G. Buchheit, F.D. Wall, G.E. Stoner, J.P. Moran, Anodic dissolution-based mechanism for the rapid cracking, preexposure phenomenon demonstrated by aluminum-lithium-copper alloys, Corrosion, 51 (1995) 417-428.
[65] M. Esmaily, J.E. Svensson, S. Fajardo, N. Birbilis, G.S. Frankel, S. Virtanen, R. Arrabal, S. Thomas, L.G. Johansson, Fundamentals and advances in magnesium alloy corrosion, Progress in Materials Science, 89 (2017) 92-193.
[66] J.H. Nordlien, S. Ono, N. Masuko, K. Nisancioglu, A TEM investigation of naturally formed oxide films on pure magnesium, Corrosion Science, 39 (1997) 1397-1414.
[67] S. Li, A.C. Bacco, N. Birbilis, H. Cong, Passivation and potential fluctuation of Mg alloy AZ31B in alkaline environments, CORROS SCI, 112 (2016) 596-610.
[68] S. Johnston, Z. Shi, A. Atrens, The influence of pH on the corrosion rate of high-purity Mg, AZ91 and ZE41 in bicarbonate buffered Hanks' solution, CORROS SCI, 101 (2015) 182-192.
[69] K. Gusieva, C.H.J. Davies, J.R. Scully, N. Birbilis, Corrosion of magnesium alloys: the role of alloying, International Materials Reviews, 60 (2015) 169-194.
[70] A. Wander, I.J. Bush, N.M. Harrison, Stability of rocksalt polar surfaces: An ab initio study of MgO(111) and NiO(111), Physical Review B, 68 (2003) 233405.
[71] J. Wang, A.G. Kalinichev, R.J. Kirkpatrick, Effects of substrate structure and composition on the structure, dynamics, and energetics of water at mineral surfaces: A molecular dynamics modeling study, Geochimica et Cosmochimica Acta, 70 (2006) 562-582.
[72] A.M. Ali, A.H. Al-Mowali, Ceramic Expansion by Water Layers on Magnesium Oxide: AB InitioStudy, American Journal of Materials Science and Engineering, 1 (2013) 50-53.
[73] J.H. Lee, J.H. Eun, S.G. Kim, S.Y. Park, M.J. Lee, H.J. Kim, Hydration behavior of MgO single crystals and thin films, J MATER RES, 18 (2003) 2895-2903.
[74] S.O. Baumann, J. Schneider, A. Sternig, D. Thomele, S. Stankic, T. Berger, H. Grönbeck, O. Diwald, Size Effects in MgO Cube Dissolution, Langmuir, 31 (2015) 2770-2776.
[75] D.-N. Zhang, L. Zhao, J.-F. Wang, Y.-L. Li, Electronic structures and the stability of MgO surface: density functional study, Surface Review and Letters, 22 (2015) 1550037.
[76] K. Kwapień, Active sites for methane activation in MgO and Li doped MgO, in, Humboldt-Universität zu Berlin, Mathematisch-Naturwissenschaftliche Fakultät I, 2012.
[77] V.R. Choudhary, S.A.R. Mulla, M.Y. Pandit, S.T. Chaudhari, V.H. Rane, Influence of precursors of Li2O and MgO on surface and catalytic properties of Li-promoted MgO in oxidative coupling of methane, Journal of Chemical Technology & Biotechnology, 75 (2000) 828-834.
[78] Y. Kuo, F. Behrendt, M. Lerch, Effect of the Specific Surface Area of Li/MgO Catalysts in the Oxidative Coupling of Methane, Zeitschrift für Physikalische Chemie, 221 (2007) 1017-1037.
[79] C.Q. Li, D.K. Xu, X.-B. Chen, B.J. Wang, R.Z. Wu, E.H. Han, N. Birbilis, Composition and microstructure dependent corrosion

behaviour of Mg-Li alloys, Electrochimica Acta, 260 (2018) 55-64.
[80] N.B. Pilling, The Oxidation of Metals at High Temperature, J. Inst. Met., 29 (1923) 529-582.
[81] A. Białobrzeski, K. Saja, K. Hubner, Ultralight magnesium-lithium alloys, Archives of Foundry Engineering, 7 (2007) 7-10.
[82] I.C. Chisem, W. Jones, Ion-exchange properties of lithium aluminium layered double hydroxides, Journal of Materials Chemistry, 4 (1994) 1737-1744.
[83] Q. Hu, L. Lei, X. Jiang, Z.C. Feng, M. Tang, D. He, Li ion diffusion in LiAlO2 investigated by Raman spectroscopy, Solid State Sciences, 37 (2014) 103-107.
[84] W.W. Rudolph, G.T. Hefter, Quantitative analysis in alkaline aluminate solutions by Raman spectroscopy, Analytical Methods, 1 (2009) 132-138.
[85] M. Mishra, P. Kuppusami, T.N. Sairam, A. Singh, E. Mohandas, Effect of substrate temperature and oxygen partial pressure on microstructure and optical properties of pulsed laser deposited yttrium oxide thin films, Applied Surface Science, 257 (2011) 7665-7670.
[86] R.J. Capwell, Raman spectra of crystalline and molten MgCl2, Chemical Physics Letters, 12 (1972) 443-446.

Tables :

Table 1. The compounds identified by in-situ Raman on the "Type 2" cathodic areas of an Mg-Li(-Al-Y-Zr) alloy in 0.1 M NaCl aqueous solution.

Compound	Experimental Raman shifts (cm^{-1})	Reference for identification
$Mg(OH)_2$	280, 444, 3652	[38]
$[(LiAl_2(OH)_6^+)_2]CO_3^{2-}$ nH_2O	557, 730, 1054	[82]
$LiAlO_2$	507, 814	[83]
$[Al(OH)_4]^-$	643, 967	[84]
Li-doped MgO-Al_2O_3	592, 1060	[42]
Y_2O_3	378	[85]
$MgCl_2$	243	[86]

Table 2. The ratio between the concentrations of soluble Mg and Li (Mg:Li ratio) detected by real time solution analysis in different exposure conditions of Mg-Li(-Al-Y-Zr) in 0.01 M NaCl solution.

Test condition / initial surface state	ratio Mg : Li in solution
1. AESEC at 200 s of OCP / fresh polished sample	2 : 1
2. AESEC at 2000 s of OCP / fresh polished sample	1.7 : 1
3. AESEC at 1200 s of anodic polarization / fresh polished then 2000 s of OCP	1.07 : 1
4. AESEC / sample preliminary immersed for 20 hours in stagnant solution	10.65 : 1
5. Solution used for 20 hours of immersion (after the sample removal)	1.21 : 1

Figure captions.

Fig. 1. Surface evolution of Mg-Li(-Al-Y-Zr) alloy during immersion in 0.1 M NaCl solution evidenced by optical microscopy and confocal Raman mapping. (a) surface appearance and spatial distribution of Li-Al-LDH (peak at 1054 cm^{-1} in Raman spectra) and $Mg(OH)_2$ (peak at 3652 cm^{-1} in Raman spectra); (b) kinetics of $Mg(OH)_2$ growth (relative thickness in arbitral units as function of time) for zones of Type 1 (no Li-Al-LDH) and Type 2 (with Li-Al-LDH). The shape of in-situ $Mg(OH)_2$ peak for zones of Type 1 and 2 are illustrated in c) and d) respectively.

Fig. 2. Evolution of the surface morphology (optical microscopy) and local chemical composition (examples of in-situ Raman spectra in points indicated by cross (spectra 1) and dot (spectra 2) respectively) during immersion of an air-exposed Mg-Li(-Al-Y-Zr) sample in 0.1 M NaCl aqueous solution. All the detected peaks belong to Li_2CO_3. Li_2CO_3 signal disappeared from all the locations on the surface after 44 minutes of immersion.

Fig. 3. Typical GD OES elemental depth profiles obtained for Mg-Li(-Al-Y-Zr) sample after immersion in 0.1 M NaCl for 20 hours: (a) tested immediately after immersion and (b) air-exposed for 3 hours between immersion and GD OES profiling.

Fig. 4. Examples of localized nano-AES spectra at different sputtered depth (a-d) and corresponding depth profiles (e) for anodic zones of Mg-Li(-Al-Y-Zr) sample (Type 1 in Fig. 1) after immersion in 0.1M NaCl. (a) Li and low energy Mg window; (b) high energy Mg window; (c) O window; (d) C window. Sputtering direction is indicated by an arrow.

Fig. 5. Elemental dissolution rates of Mg and Li, the corresponding potential and the calculated ratio between released Mg and Li measured by AESEC during reactivity of (a) a freshly polished and (b) an "immersed" Mg-Li(-Al-Y-Zr) samples in 0.01 M NaCl at 25 °C.

Fig. 6. Typical surface appearance of pure Mg after 1 h immersion in 0.1 M LiCl at initial pH 7.5 (a) and examples of photoluminescence spectra (b) collected at zones indicated as "1", "2" and "3" in (a) compared with the spectrum collected on the pure Mg after 1 h immersion in 0.1 M NaCl with initial pH 7.5.

Fig. 7. Schematic representation of steps of aqueous corrosion of Mg-Li alloy: selective dissolution of Li^+ (1); diffusion of Mg^{2+} via MgO and dissolution of Mg^{2+} (2); doping of MgO by Li^+ (3);; corrosion products formation around cathodic sites (4). Dash-lined red and black circles represent Li and Mg atoms in different steps, the dash-filled circle indicates ionic and white filled indicates metallic state.

Fig. 8. Schematic representation of (a) common and (b) specific for Li-doped charge compensation mechanisms in Mg_1O_{1-X}: adsorption of aggressive anions (1), surface hydroxylation (2), oxide dissolution (3), electron trapped by cathodic catalysis (4) and charge compensation via doping by Li^+ (5). The figure illustrates an example of F^{2+} centre, represented in Kröger–Vink notation ($[V_O^{\bullet\bullet}]$); δ^+ and δ^{++} indicate the positive surface charge, assuming higher charge for δ^{++}.

Fig. 9. Influence of Li content in the alloy on the calculated Pilling Bedford (PB) ratio assuming a Li-doped MgO. See text for details of calculation. PB ratio >1 is considered as indication of a passivating surface films.

Figures:

Fig. 1

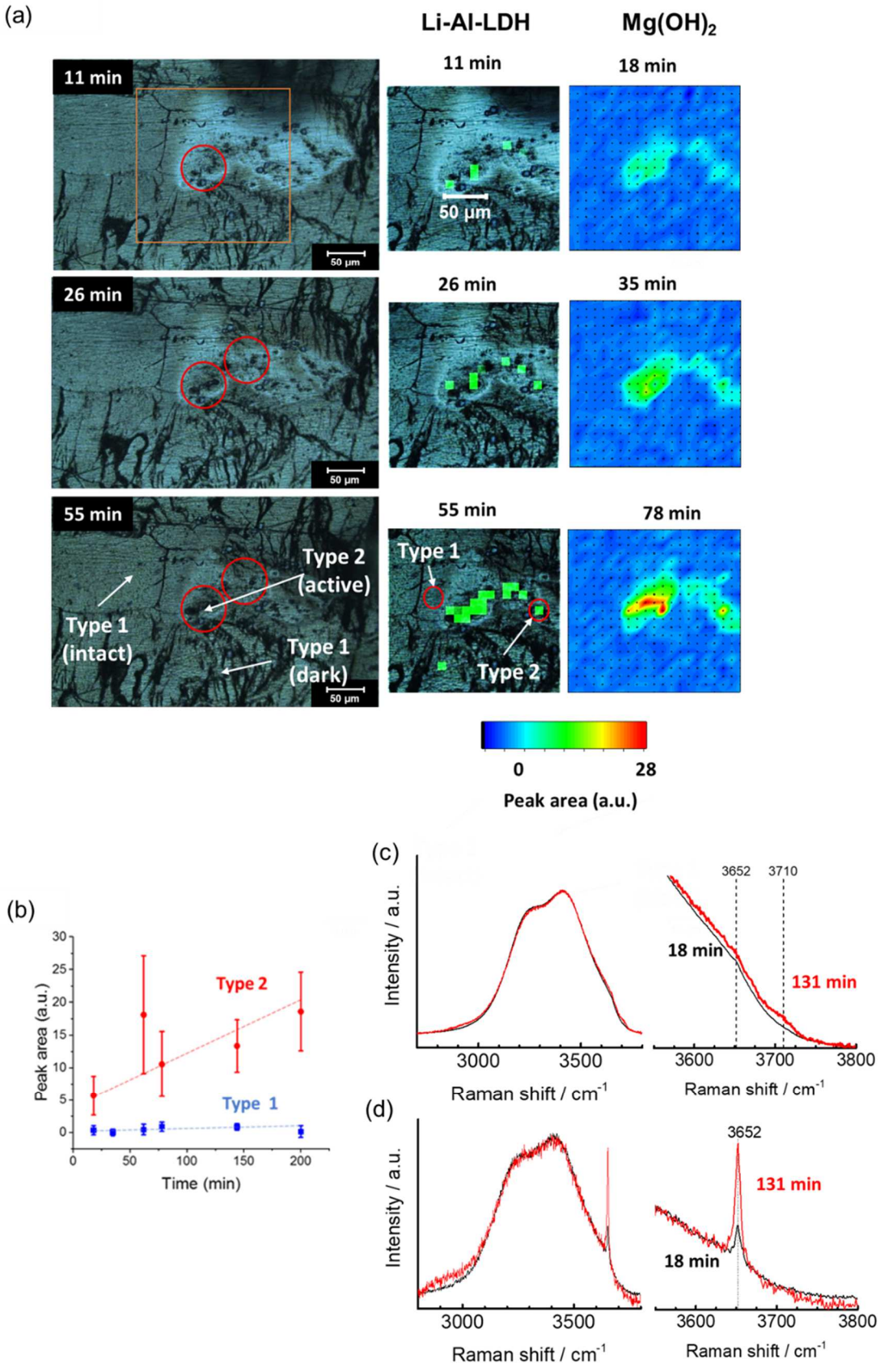

Fig. 2

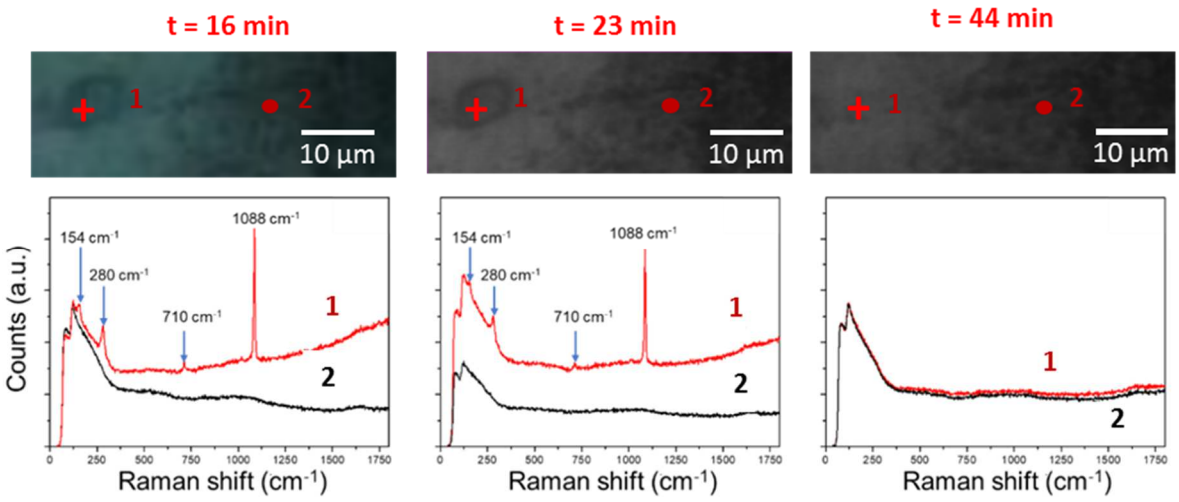
t = 16 min
t = 23 min
t = 44 min
1
2
10 µm
154 cm-1
280 cm-1
710 cm-1
1088 cm-1
Counts (a.u.)
Raman shift (cm-1)

Fig. 3

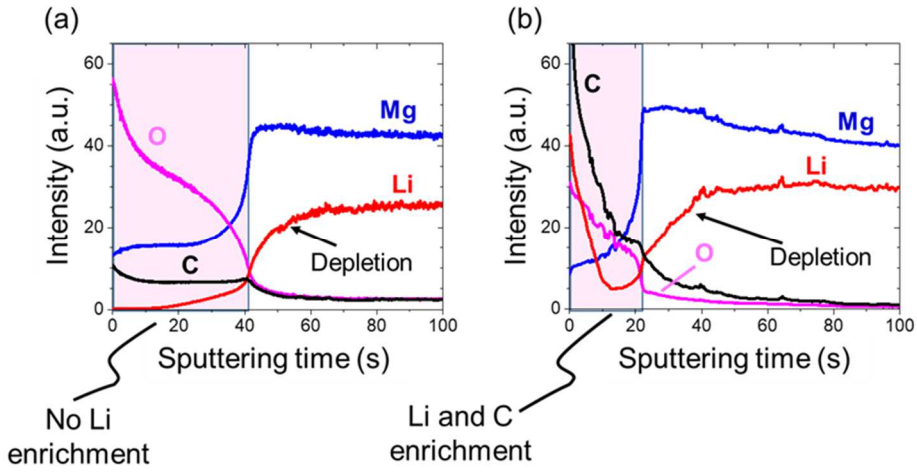
(a)
(b)
Intensity (a.u.)
Sputtering time (s)
Mg
Li
O
C
Depletion
No Li enrichment
Li and C enrichment

Fig. 4.

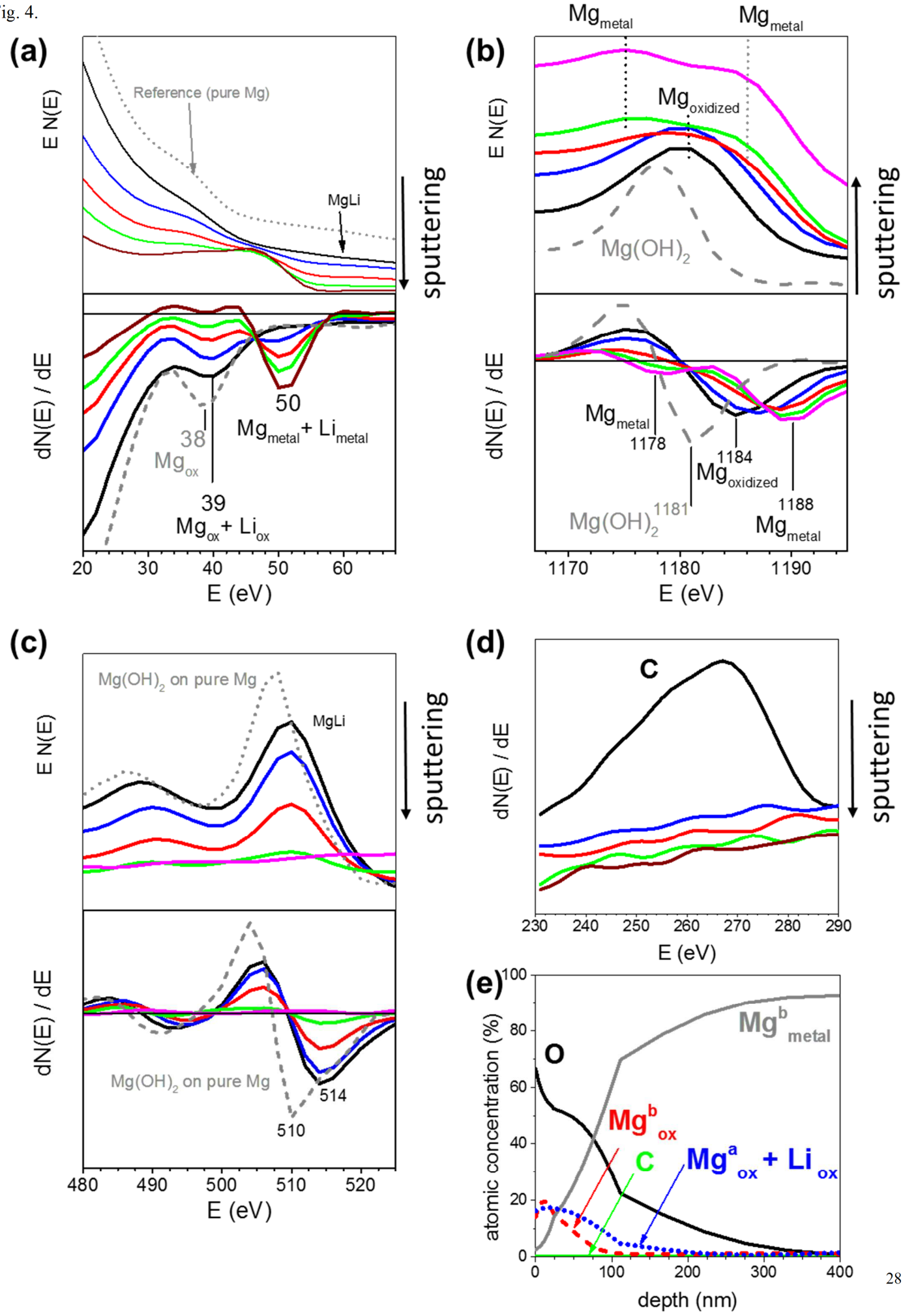
(a)
E N(E)
Reference (pure Mg)
MgLi
sputtering
dN(E) / dE
50
Mg_metal + Li_metal
38
Mg_ox
39
Mg_ox + Li_ox
20
30
40
50
60
E (eV)
(b)
Mg_metal
Mg_metal
Mg_oxidized
Mg(OH)_2
E N(E)
sputtering
dN(E) / dE
Mg_metal
1178
1184
Mg_oxidized
Mg(OH)_2
1181
1188
Mg_metal
1170
1180
1190
E (eV)
(c)
Mg(OH)_2 on pure Mg
MgLi
E N(E)
sputtering
dN(E) / dE
Mg(OH)_2 on pure Mg
514
510
480
490
500
510
520
E (eV)
(d)
C
dN(E) / dE
sputtering
230
240
250
260
270
280
290
E (eV)
(e)
100
80
60
40
20
0
atomic concentration (%)
O
Mg^b metal
Mg^b ox
C
Mg^a ox + Li ox
0
100
200
300
400
depth (nm)

Fig. 5

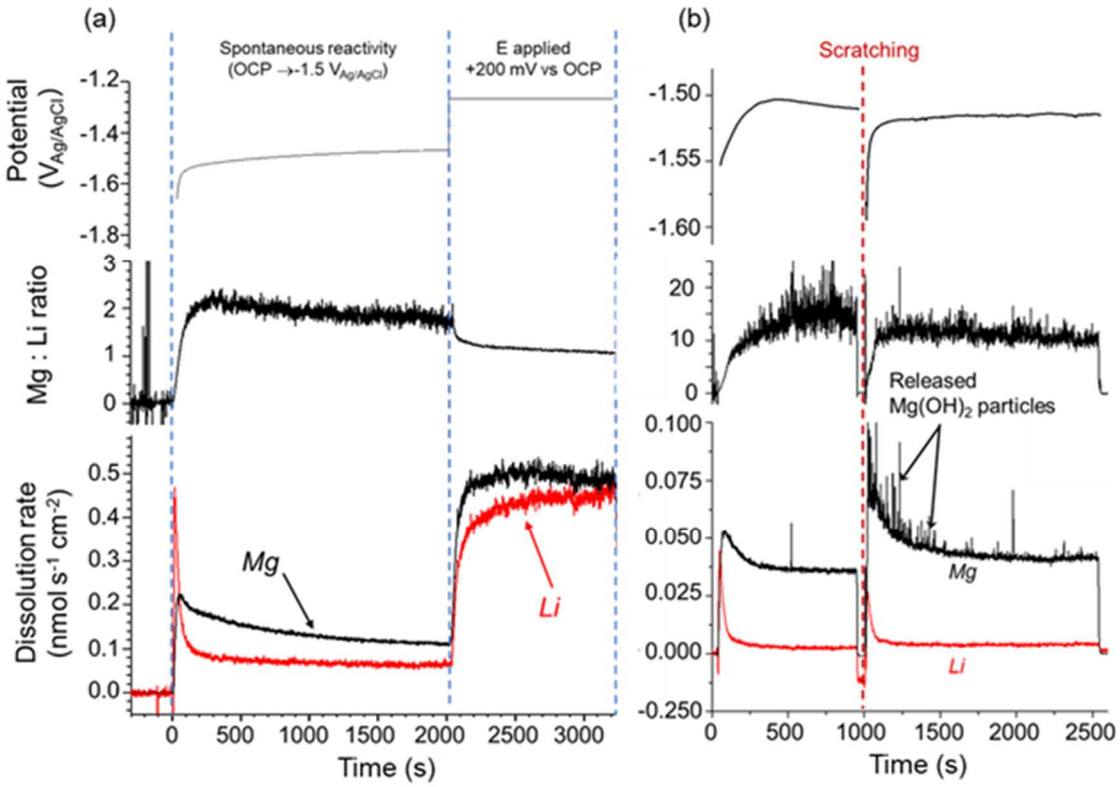
(a)
Spontaneous reactivity
(OCP →-1.5 V$_{Ag/AgCl}$)
E applied
+200 mV vs OCP
Potential (V$_{Ag/AgCl}$)
Mg : Li ratio
Dissolution rate (nmol s^{-1} cm^{-2})
Mg
Li
Time (s)
(b)
Scratching
Released Mg(OH)$_2$ particles
Mg
Li
Time (s)

Fig. 6.

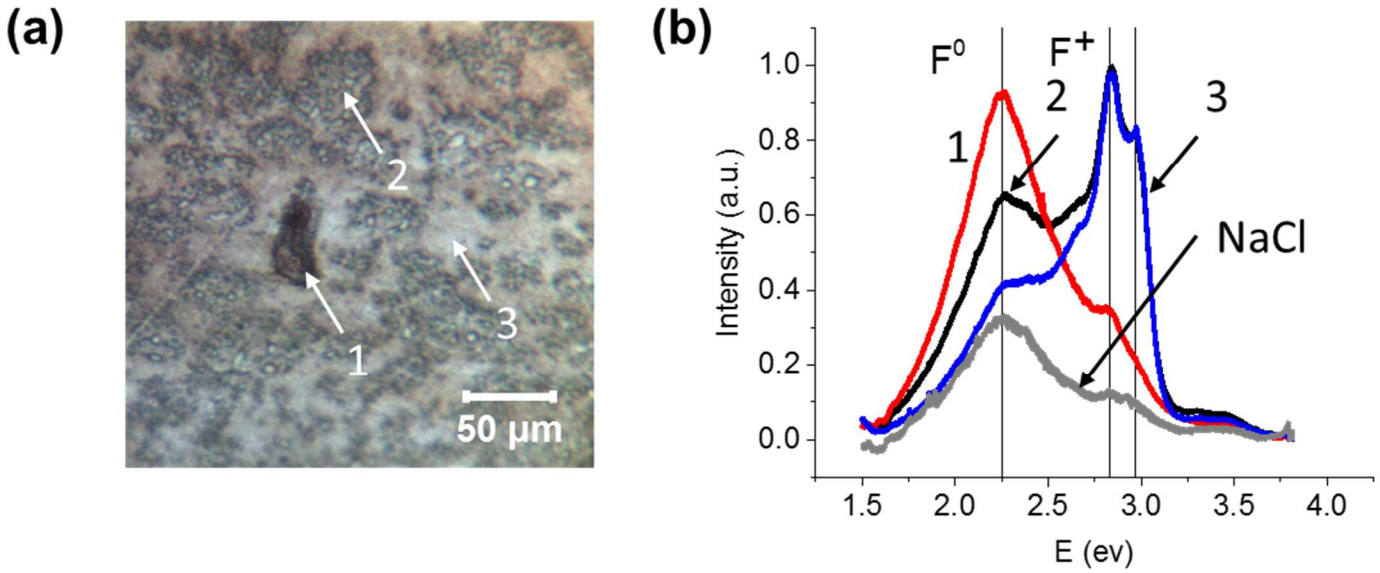
(a)
1
2
3
50 µm
(b)
F^0
F$^+$
1
2
3
NaCl
Intensity (a.u.)
E (ev)

Fig. 7.

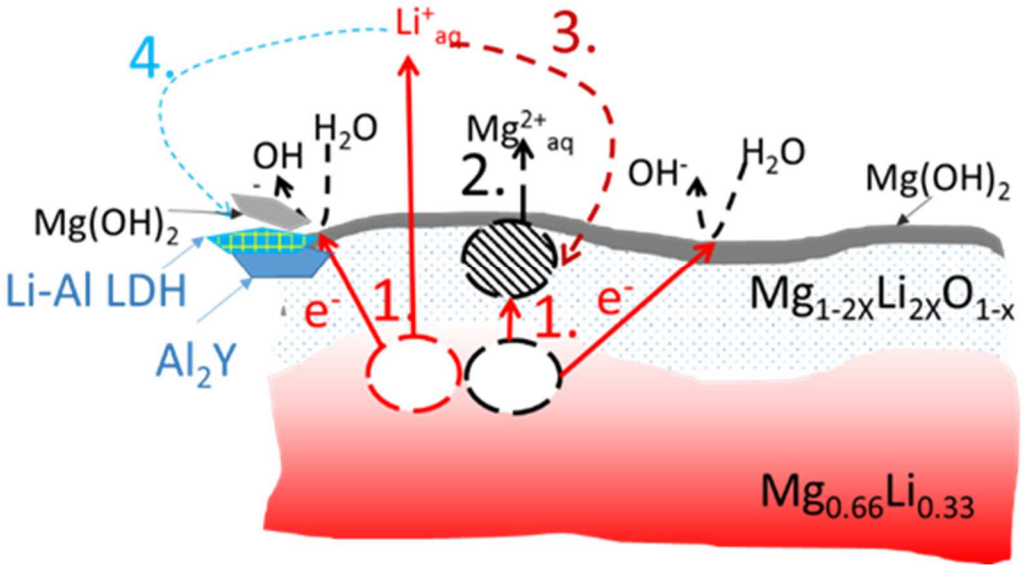
Li+ aq
4.
3.
OH-
H2O
Mg2+ aq
2.
OH-
H2O
Mg(OH)2
Mg(OH)2
Li-Al LDH
Al2Y
e-
1.
1.
e-
Mg1-2XLi2XO1-x
Mg0.66Li0.33

Fig. 8.

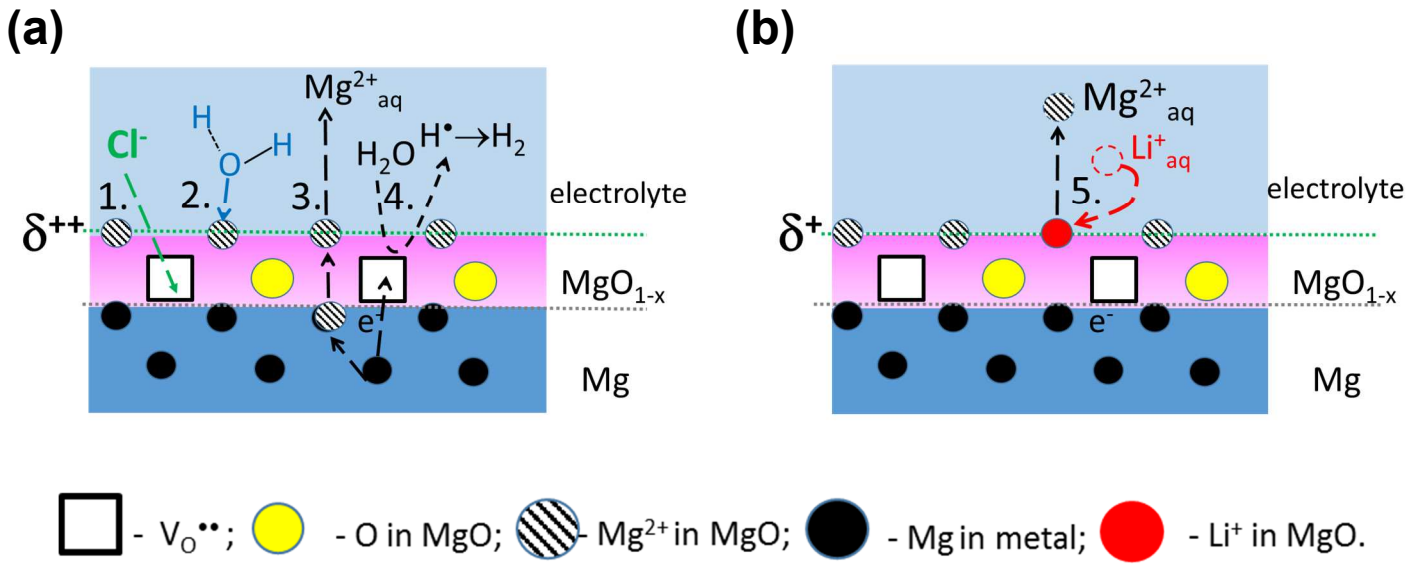
(a)
Cl-
H
O
H
Mg2+ aq
H2O
H•→H2
1.
2.
3.
4.
δ++
electrolyte
MgO1-x
e-
Mg
(b)
Mg2+ aq
Li+ aq
5.
δ+
electrolyte
MgO1-x
e-
Mg
- VO••; - O in MgO; - Mg2+ in MgO; - Mg in metal; - Li+ in MgO.

Fig. 9.

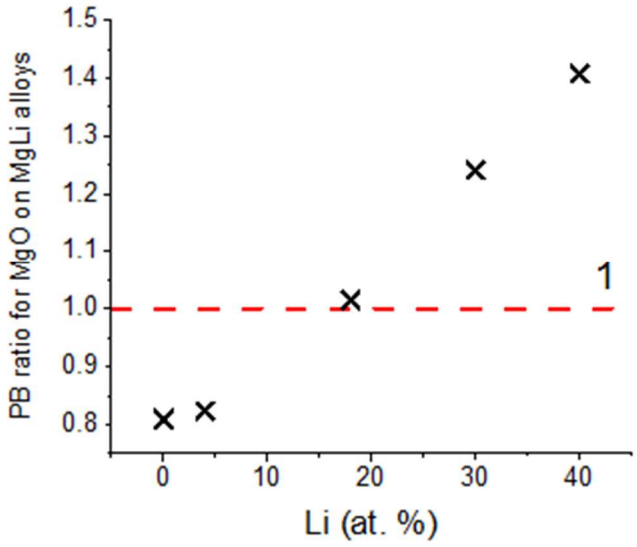
PB ratio for MgO on MgLi alloys
1.5
1.4
1.3
1.2
1.1
1.0
0.9
0.8
1
0
10
20
30
40
Li (at. %)
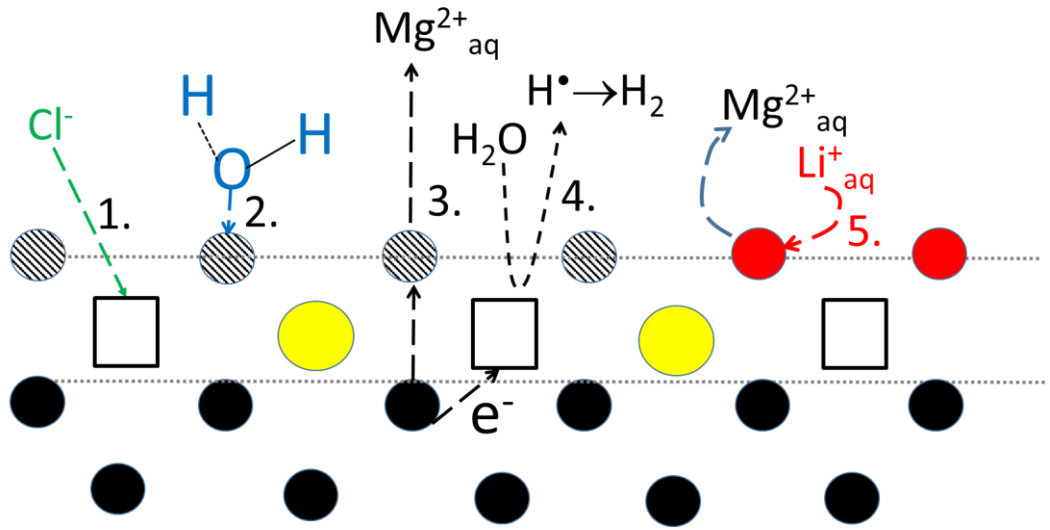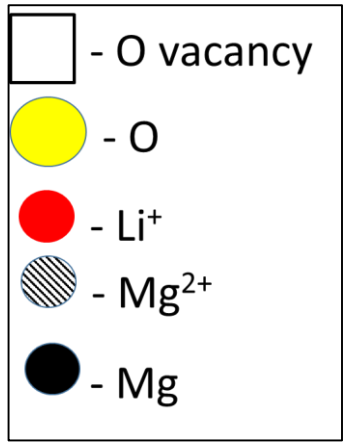
Competitive charge compensation mechanisms affecting aqueous stability of Mg-Li alloys